(Received 22 April 2025, Accepted 1 July 2025, Scheduled 15 July 2025)

A Composite Sliding Mode Control for PMSM Drives Based on an Adaptive Reaching Law with Disturbance Compensation

Pengpeng Liu[1], Zhonggen Wang[1,*], and Wenyan Nie[2]

[1] *School of Electrical and Information Engineering, Anhui University of Science and Technology, Huainan 232001, China*
[2] *School of Mechanical and Electrical Engineering, Huainan Normal University, Huainan 232001, China*

ABSTRACT: To address internal parameter ingress and external load perturbations in the speed loop of a permanent magnet synchronous motor (PMSM) and enhance the dynamic performance and robustness of its speed control system, this study proposes a novel adaptive sliding mode reaching law-based controller integrated with a global non-singular fast terminal sliding mode observer (GNFTSMO). The proposed reaching law incorporates system state variables as power functions, thereby minimizing steady-state errors and resolving the inherent trade-off between chatter suppression and rapid response. To further enhance the dynamic and steady-state performance of the PMSM control system, a GNFTSMO is designed. This observer reduces the switching gain of the convergence law while incorporating feed-forward compensation for perturbations, thereby improving the system's anti-disturbance capability. The feasibility and effectiveness of the proposed sliding mode control method are empirically validated through both simulation and experimental studies.

1. INTRODUCTION

Permanent Magnet Synchronous Motors (PMSMs) are extensively utilized in urban rail transit, electric vehicles, wind power generation, and related applications due to their high performance, high-power density, and structural simplicity [1–4]. Conventional PMSM speed control systems typically employ traditional proportional-integral (PI) control, leveraging its algorithmic simplicity, ease of implementation, and straightforward tuning, making it a common choice for linear control systems. However, practical PMSM speed control systems exhibit nonlinearity, strong coupling, and multivariable dynamics, rendering linear control methods like PI algorithm insufficient for achieving both rapid response and robust performance [5, 6].

To enhance the performance of PMSM speed control systems, more and more high-performance and high-precision control strategies have been proposed in recent years including fuzzy control [7, 8], self-resilient control [9], adaptive control [10], sliding-mode control (SMC) [11], and many other advanced nonlinear control theories have been successfully applied to the speed control system of PMSM. In comparison to other methods, SMC has gained prominence in PMSM speed control systems due to its rapid dynamic response and inherent robustness [9]. However, the predominant use of linear sliding mode surfaces in SMC prevents finite-time convergence to equilibrium, thereby limiting its practical applicability [12]. Nonlinear sliding mode surfaces have been widely adopted to enhance the dynamic performance of SMC systems compared to their linear counterparts. The Terminal Sliding Mode Controller, among the earliest strategies employing nonlinear surfaces, enables finite-time convergence of system states to steady-state conditions [13–15]. However, singularity-induced control input divergence has restricted its practical implementation. To address this, [16] proposed a non-singular terminal sliding mode controller, accelerating the system's response time and mitigating chattering through singularity avoidance.

The chattering phenomenon stems from non-ideal convergence of the system trajectory toward the sliding mode surface. The effectiveness of this convergence process, governed by the design of the reaching law, highlights the necessity of advanced reaching laws to suppress chattering. In [17], a power term integrated with system state variables is constrained by the absolute value of the switching function, reducing chattering while accelerating convergence to the sliding mode surface. In [18], replacing the switching function with a saturation function attenuates chattering but compromises convergence speed and system robustness. Alternative strategies integrate SMC with auxiliary algorithms to optimize convergence dynamics. In [19], a reaching law fused with particle swarm optimization enables an intelligent second-order sliding mode controller that achieves robust disturbance rejection. However, practical deployment faces limitations, including computational complexity and sensitivity to parameter tuning [20]. The aforementioned methods may compromise the steady-state accuracy of system state variables under external disturbances. Moreover, the approach to reaching law effectively attenuates chattering under conditions of limited disturbance magnitude. However, for substantial or bound-unknown disturbances, reaching law design necessitates sufficiently large switching gains to ensure robust disturbance rejection, inevitably exacerbating SMC. Conversely, insufficient switching gains impair the system's robustness and disturbance rejection capabilities.

To address these challenges, a widely adopted strategy integrates SMC with disturbance observers to enhance system ro-

* Corresponding author: Zhonggen Wang (zgwang@ahu.edu.cn).

bustness. In [21], a disturbance observer (DO) was developed to account for both parametric uncertainties and external disturbances in PMSM speed control systems. In [22], a composite controller integrating a novel disturbance observer (NDO) with SMC was designed, leveraging a composite barrier function to achieve superior dynamic performance in PMSM speed regulation. In contrast to DO-based methods, sliding mode observer (SMO)-based approaches exhibit enhanced disturbance rejection, reduced sensitivity to parameter variations, and simplified parameter tuning [23].

To enhance the dynamic performance and robustness of PMSM speed control systems, this work proposes an adaptive sliding mode reaching law (ASMRL) controller integrated with a global non-singular fast terminal SMO (GNFTSMO). The principal contributions of this study are threefold:

(1) A novel ASMRL is proposed to optimize the speed controller. Theoretical analysis demonstrates that ASMRL reduces convergence time while resolving the inherent trade-off between rapid convergence and chattering suppression.

(2) A GNFTSMO, grounded in a non-singular fast terminal sliding mode surface, is designed to observe and compensate for aggregate disturbances, thereby enhancing the system's anti-disturbance capability particularly critical in complex dynamic operating conditions.

(3) Several sets of experiments are designed to verify that the proposed anti-disturbance controller based on the ASMRL-GNFTSMO has better dynamic and steady-state characteristics.

2. DYNAMIC MATHEMATICAL MODEL OF PMSM

Assuming symmetrical windings and neglecting core saturation and disregarding eddy current losses and hysteresis losses, the mathematical model of a PMSM can be obtained according to the motor control theory in [2]. The mathematical model of PMSM in a d-q synchronous reference frame can be written as [4]:

$$\begin{cases} u_d = Ri_d - L_q i_q p_n \omega_m + L_d \dfrac{di_d}{dt} \\ u_q = Ri_q + +(L_d i_d + \psi_f) p_n \omega_m + L_q \dfrac{di_q}{dt} \\ T_e = \dfrac{3}{2} P_n i_q \left[(L_d - L_q) i_d + \psi_f \right] \\ J \dfrac{d\omega_m}{dt} = T_e - T_L - B\omega_m \end{cases} \tag{1}$$

where u_d and u_q, i_d and i_q, L_d and L_q denote the d-q axis stator voltages, stator currents, and stator inductances, respectively; R is the stator resistance; ω_m is the mechanical angular speed; P_n and ψ_f represent the number of pole pairs and flux linkage of permanent magnet, respectively; J and B are the motor inertia and viscous friction coefficients, respectively; T_e is the electromagnetic torque; T_L is the load torque.

For surface mounted PMSM (SPMSM), the inductance in d axis equals that in q axis ($L_d = L_q$). Therefore, Eq. (1) can be replaced by:

$$\begin{cases} \dfrac{di_q}{dt} = \dfrac{1}{L_q}(-Ri_q - P_n \omega_m \psi_f + u_q) \\ J \dfrac{d\omega_m}{dt} = \dfrac{3}{2} P_n \psi_f i_q - T_L - B\omega_m \end{cases} \tag{2}$$

3. SLIDING MODE CONTROL BASED ON AN ADAPTIVE REACHING LAW

3.1. Existing Sliding-mode Reaching Law

SMC is a variable structure control method that is inherently nonlinear. The following general nonlinear second-order dynamic system is widely employed to describe SMC systems utilizing reaching law approaches. Consider a nonlinear second-order dynamic system:

$$\begin{cases} \dot{x}_1 = x_2 \\ \dot{x}_2 = f(x) + g(x)u + d(x) \end{cases} \tag{3}$$

where $x = [x_1, x_2]^T$ is the state variable, u the control input, $f(x)$ the system function, $g(x)$ the input function, $d(x)$ represents the entire system disturbance, and $d(x)$ bounded.

The design of the SMC is divided into two steps. Firstly, SMC should ensure that the system state reaches the surface of the sliding mode and the stability of the controller, with the traditional sliding mold surface (TSMS) selected as:

$$s = cx_1 + x_2 \tag{4}$$

where c is a constant that satisfies the Hurwitz condition.

The derivation of s gives:

$$\begin{aligned} \dot{s} &= c\dot{x}_1 + \dot{x}_2 \\ &= cx_2 + f(x) + g(x)u + d(x) \end{aligned} \tag{5}$$

The second step in the sliding mode control process is the design of the sliding mode reach law, a well-defined reach law ensures the dynamic quality of the convergent motion of the system. The traditional sliding mode reaching law (TSMRL) [24] is defined as:

$$\dot{s} = -k_1 \text{sign}(s) - k_2 s \tag{6}$$

where k_1 and k_2 are parameters to be determined, and $k_1 > 0$, $k_2 > 0$.

The reference sliding mode reaching law (RSMRL) is studied in [25] as:

$$\dot{s} = -k_1 |x|^a \tanh(\lambda s) - k_2 s \left(\alpha |s|^b + \frac{\beta}{|s|^b} \right) \tag{7}$$

where x denotes the system state and $\lim_{t \to \infty} |x| = 0$. k_1, k_2, a, b, α, β are parameters to be determined, and $k_1 > 0$, $k_2 > 0$, $1 > a > 0$, $1 > b > 0$, $\alpha > \beta > 0$.

According to Eqs. (3)–(6), the controller is designed as:

$$u = \frac{1}{g(x)}\left(-cx_2 - f(x) - d(x) - k_1 \text{sign}(s) - k_2 s\right) \quad (8)$$

Integrating both sides of Eq. (6) with $s(t) = 0$ at time t, the convergence time of the state variable is as:

$$t = \frac{1}{k_1} \ln\left(1 + \frac{k_1}{k_2}|s_0|\right) \quad (9)$$

where s_0 is the initial state of s.

Integrating both sides of Eq. (7) with $s(t) = 0$ at time t, the convergence time of the state variable is as:

$$t = \frac{|s_0|^{1-b}}{k_2\alpha(1-b)} + \frac{C}{k_2\beta(1+b)} \quad (10)$$

where C is a constant indicating the state amplitude of the switching point.

The above equation leads to the conclusion that t varies with the variation of parameters in the reaching law. In the TSMRL, increasing the velocity term can reduce the time to reach the sliding mode surface. However, when the error between the system's initial state and estimated state is large, the velocity term drives the reaching law toward the sliding mode surface with a fixed gain. Since it cannot be adaptively adjusted according to the system state, this will lead to severe chattering and large deviations in the system. The introduction of system state variables can effectively weaken the effect of jitter, but the convergence time will be affected by s and x. In addition, the introduction of state variable coefficients into the velocity term will weaken the anti-disturbance performance of the RSMRL.

3.2. Proposed Adaptive Sliding Mode Reaching Law

To resolve the above problem of the sliding mode reaching law, this paper proposes a state variable-based ASMRL:

$$\begin{cases} \dot{s} = -k_1 |s|^{\alpha_1 - \frac{1}{b_1+|x|}} \tanh(\lambda s) - k_2 |s|^{\alpha_2 + \frac{1}{b_2+|x|}} s \\ \lim\limits_{t\to\infty} |x| = 0 \end{cases} \quad (11)$$

where x denotes the system state; k_1, k_2, α_1, α_2, b_1, b_2, λ are the positive constants and $0 < \alpha_1 < 1$, $0 < \alpha_2 < 1$, $0 < b_1$, $0 < b_2$, $0 < \lambda$, and $\alpha_1 < 1/b_1$, $-1/b_2 < \alpha_2$ preventing system divergence or convergence failure.

The reaching law consists of two parts: the power term $-k_1 |s|^{\alpha_1 - \frac{1}{b_1+|x|}} \tanh(\lambda s)$ and the power term $-k_2 |s|^{\alpha_2 + \frac{1}{b_2+|x|}} s$ based on the state variables. When the system is far away from the sliding mode surface $s = 0$, i.e., $|s| > 1$, the power term $-k_2 |s|^{\alpha_2 + \frac{1}{b_2+|x|}} s$ plays the main role, at this time $k_2 |s|^{\alpha_2 + \frac{1}{b_2+|x|}} s > k_2 s$ and $k_1 |s|^{\alpha_1 - \frac{1}{b_1+|x|}} > k_1$, which indicates that the reaching law proposed in this paper is faster than the traditional reaching law in this stage, ensuring that the system arrives at the sliding mode surface quickly; when the system state is close to the sliding mode surface, i.e., $|s| < 1$, the power convergence term $-k_1 |s|^{\alpha_1 - \frac{1}{b_1+|x|}} \tanh(\lambda s)$ plays the main role, and at this time there are $k_1 |s|^{\alpha_1 - \frac{1}{b_1+|x|}} < k_1$ and $k_2 |s|^{\alpha_2 + \frac{1}{b_2+|x|}} s < k_2 s$. The ASMRL adaptively adjusts as the system state x diminishes, mitigating chattering induced by fixed velocity term coefficients. Additionally, the sign function sign(s) is substituted with the hyperbolic tangent function $\tanh(\lambda s)$, further attenuating chattering. Fig. 1 illustrates the comparative profiles of $\tanh(\lambda s)$ and sign(s). As illustrated, reducing λ enhances the smoothness of the reaching law, thereby minimizing chattering.

$$\tanh(\lambda s) = 1 - \frac{2}{1 + e^{\lambda s}} \quad (12)$$

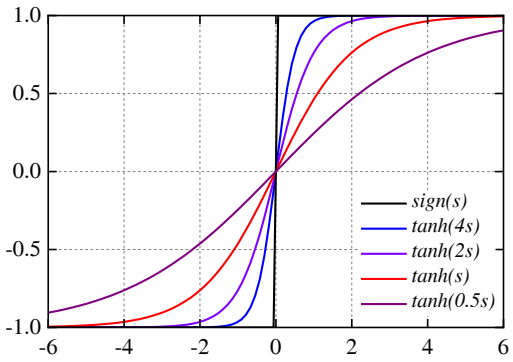

FIGURE 1. Images of $\tanh(\lambda s)$ and $\text{sign}(s)$.

3.3. Convergence Time Analysis of the ASMRL

Theorem 1: The state of the system under the action of ASMRL can reach the sliding mode surface $s = 0$ from any position s in finite time $t_{s_0\to 0}$ when $|x_0| > 0$ [25].

Proof: Define $V = 0.5s^2$; combined with (11), the derivative of V can be calculated as:

$$\begin{aligned} \dot{V} = s\dot{s} &= s\left[-k_1 |s|^{\alpha_1 - \frac{1}{b_1+|x|}} \tanh(\lambda s) - k_2 |s|^{\alpha_2 + \frac{1}{b_2+|x|}} s\right] \\ &= -k_1 |s|^{\alpha_1 - \frac{1}{b_1+|x|}+1} - k_2 |s|^{\alpha_2 + \frac{1}{b_2+|x|}+2} \le 0 \end{aligned} \quad (13)$$

In summary, there is $s\dot{s} = 0$ if and only if $s = 0$. It follows that the convergence law exists and is reachable, and the system can reach the equilibrium point under the action of Eq. (11).

Assuming an initial state of the system $s(0) > 1$, a finite time calculation is performed in two stages.

Process 1: In $s(0) \to s = 1$ process, the power term $-k_2 |s|^{\alpha_2 + \frac{1}{b_2+|x|}} s$ acts much more than the power term $-k_1 |s|^{\alpha_1 - \frac{1}{b_1+|x|}} \tanh(\lambda s)$, and only the power term

$-k_2 |s|^{\alpha_2+\frac{1}{b_2+|x|}} s$ is considered. At this time, the exponent $\alpha_2+\frac{1}{b_2+|x|}$ follows $|x| \to 0$ which tends to $\alpha_2+\frac{1}{b_2}$.

$$\dot{s}_1 = -k_2 |s|^{\alpha_2+\frac{1}{b_2}+1} \tag{14}$$

The convergence time of the state variables can be derived by integrating Eq. (14) as:

$$t_1 = \frac{1-s(0)^{-\left(\alpha_2+\frac{1}{b_2}\right)}}{k_2\left(\alpha_2+\frac{1}{b_2}\right)} \tag{15}$$

Process 2: In $s = 1 \to s = 0$ process, the power term $-k_1 |s|^{\alpha_1-\frac{1}{b_1+|x|}} \tanh(\lambda s)$ acts much more than the power term $-k_2 |s|^{\alpha_2+\frac{1}{b_2+|x|}} s$, and only the power term $-k_1 |s|^{\alpha_1-\frac{1}{b_1+|x|}} \tanh(\lambda s)$ is considered. At this time, the exponent $\alpha_1-\frac{1}{b_1+|x|}$ follows $|x| \to 0$ which tends to $\alpha_1-\frac{1}{b_1}$.

$$\dot{s}_2 = -k_1 |s|^{\alpha_1-\frac{1}{b_1}} \tag{16}$$

The convergence time of the state variables can be derived by integrating Eq. (16) as:

$$t_2 = \frac{1}{k_1\left(1-\alpha_1+\frac{1}{b_1}\right)} \tag{17}$$

The sum of the time required for the two processes as:

$$t = \frac{1-s(0)^{-\left(\alpha_2+\frac{1}{b_2}\right)}}{k_2\left(\alpha_2+\frac{1}{b_2}\right)} + \frac{1}{k_1\left(1-\alpha_1+\frac{1}{b_1}\right)} \tag{18}$$

When $s(0) < -1$, one has:

$$t = \frac{1+s(0)^{-\left(\alpha_2+\frac{1}{b_2}\right)}}{k_2\left(\alpha_2+\frac{1}{b_2}\right)} + \frac{1}{k_1\left(1-\alpha_1+\frac{1}{b_1}\right)} \tag{19}$$

where t represents the cumulative convergence time of dominant power terms active during distinct operational stages. Finite-time convergence analysis ensures that the system state reaches equilibrium from any initial condition within a bounded time frame. Therefore, the actual ASMRL convergence time is less than Eqs. (18) and (19).

3.4. Analysis of Steady-State Error Bounds in the Presence of ASMRL Perturbations

The analysis of ASMRL demonstrates finite-time convergence to the equilibrium point. However, under external bounded uncertain disturbances, the system converges only to a neighborhood of (0, 0) via the reaching law, defining the perturbed steady-state boundary.

In the general nonlinear second-order dynamical system Eq. (3), it is assumed that $f(x)$ and $g(x)$ are bounded nonlinear matrix functions of the state of the system, respectively, and $|d(x)| \le M$. The equivalent ASMRL-based control law can be obtained as:

$$u = \frac{1}{g(x)}\left(-cx_2 - f(x) - k_1 |s|^p \tanh(\lambda s) - k_2 |s|^q s\right) \tag{20}$$

where $p = \alpha_1 - \frac{1}{b_1+|x|} q = \alpha_2 + \frac{1}{b_2+|x|}$.

Substituting Eq. (20) into Eq. (5) gives:

$$\dot{s} = -k_1 |s|^p \tanh(\lambda s) - k_2 |s|^q s + d(x) \tag{21}$$

Lemma 1: Assume that the system state $x \in D \subset R^n$, and $\dot{x} = f(x)\, f : R^n \to R^n$ are continuous functions defined in the domain D of the equilibrium point, and assume that the continuous functions satisfy the following conditions: ① V is positive definite; ② $\dot{V}$ is negative definite except at the equilibrium point; and ③ there exist a domain $M \subset D$ and a real number $\alpha > 0$, $\beta > 0$ such that $\dot{V} + \alpha V^\beta \le 0$, then $\dot{x} = f(x)$ converges at the equilibrium point in finite time [26].

Theorem 2: The system states s and $\dot{s}$ converge in finite time to the following region.

$$|s| \le \min\left(\left(\frac{M}{K_1}\right)^{1/p}, \left(\frac{M}{K_2}\right)^{1/q}\right) \tag{22}$$

$$|\dot{s}| \le \min\left(K_1\left(\frac{M}{K_2}\right)^{p/q}, M\right) + \min\left(M, K_2\left(\frac{M}{K_1}\right)^{q/p}\right) + M \tag{23}$$

Proof: According to the Lyapunov function, the derivation of V along Eq. (4) leads to:

$$\begin{aligned}\dot{V} &= s\dot{s} = s(u + d(x)) \\ &= s(-k_1 |s|^p \tanh(\lambda s) - k_2 |s|^q s + d(x)) \\ &= -k_1 |s|^p s - k_2 |s|^q s^2 + d(x) s \\ &\le -k_1 |s|^{p+1} - k_2 |s|^{q+2} + M |s|\end{aligned} \tag{24}$$

Eq. (24) can be rewritten as:

$$\begin{aligned}\dot{V} &\le -k_1 |s|^{p+1} - k_2 |s|^{q+2} s + M |s| \\ &= -(k_1 |s|^p - M) |s| - k_2 |s|^{q+2}\end{aligned} \tag{25}$$

When satisfying $k_1 |s|^p - M \ge 0$, it follows that:

$$\dot{V} \le -k_2 |s|^{q+2} = -k_2 s (2V)^{(2+q)/2} \tag{26}$$

Therefore, according to Lemma 1 the system converges in finite time with the region of convergence as:

$$|s| \le \left(\frac{M}{K_1}\right)^{1/p} \tag{27}$$

Convergence of the system can be ensured. Eq. (2) can also be rewritten as:

$$\dot{V} \le -k_1 |s|^{p+1} - k_2 |s|^{q+2} + M |s|$$

$$= -\left(k_2 |s|^{q+1} - M\right) |s| - k_1 |s|^{p+1} \quad (28)$$

Similarly, when satisfying $k_2 |s|^q s - M \geq 0$, it follows that:

$$\dot{V} \leq -k_1 |s|^{p+1} = -k_1 (2V)^{(1+p)/2} \quad (29)$$

Hence, by Lemma 1 the system converges in finite time with the region of convergence as:

$$|s| \leq \left(\frac{M}{K_2}\right)^{1/q} \quad (30)$$

The convergence of the system can be guaranteed. Combining Eqs. (27) and (30) yields the convergence region.

$$|s| \leq \min\left(\left(\frac{M}{K_1}\right)^{1/p}, \left(\frac{M}{K_2}\right)^{1/q}\right) \quad (31)$$

Substituting Eq. (31) into Eq. (21) gives:

$$\begin{aligned} |\dot{s}| &\leq k_1 |s|^p \tanh(\lambda s) + k_2 |s|^q s + d(x) \\ &\leq k_1 |s|^p + k_2 |s|^q s + M \\ &\leq \min\left(K_1 \left(\frac{M}{K_2}\right)^{p/q}, M\right) \\ &+ \min\left(M, K_2 \left(\frac{M}{K_1}\right)^{q/p}\right) + M \end{aligned} \quad (32)$$

To summarize, get the proof. When the system encounters a perturbation, the proffered convergence law suppresses the perturbation and reduces the steady state error.

3.5. Performance Comparison of Several Reaching Laws

The performances of the TSMRL, RSMRL, and ASMRL can be compared using the numerical analysis method. For this purpose, a second-order nonlinear model as shown in Eq. (33) is established [27].

$$\ddot{\theta}(t) = -f(\theta, t) + bu(t) + d(t) \quad (33)$$

where $f(\theta, t) = 25\dot{\theta}$ is the system position, $u(t)$ the input of controller, $b = 133$ a constant, and $d(t)$ the lumped disturbance. The derivative of Eq. (4) based on a TSMS is combined with Eq. (11) as follows:

$$\begin{aligned} \dot{s} &= c\dot{x}_1 + \dot{x}_2 = c\dot{e}(t) + \ddot{e}(t) \\ &= -k_1 |s|^{\alpha_1 - \frac{1}{b_1 + |x|}} \tanh(\lambda s) - k_2 |s|^{\alpha_2 + \frac{1}{b_2 + |x|}} s \end{aligned} \quad (34)$$

where $e(t)$ is the error, $e(t) = \theta_i(t) - \theta(t)$; $\theta_i(t)$ represents the reference position, $\theta_i(t) = \sin(t)$.

By substituting Eq. (33) into Eq. (34), the control input $u(t)$ is as:

$$u = \frac{1}{b}\left[c(\dot{\theta}_i - \dot{\theta}) + \ddot{\theta}_i + f(\theta, t) - d(t) + k_1 |s|^{\alpha_1 - \frac{1}{b_1 + |x|}} \tanh(\lambda s) + k_2 |s|^{\alpha_2 + \frac{1}{b_2 + |x|}} s\right] \quad (35)$$

Comparing the performances of TSMRL, RSMRL and ASMRL, the s-function in MATLAB is used to simulate the motor model. The parameter values are set as follows: $c = 10$, $k_1 = 15$, $k_2 = 130$, $\lambda = 1$, $\alpha_1 = \alpha_2 = b_1 = b_2 = 0.1$, the lumped disturbance set as $d(t) = 10\sin(\pi t)$, and the initial system state set as $[x_1, x_2] = [-2, -2]$, and x_1 and x_2 are the state variables of the system.

In Fig. 2, the control performances of TSMRL, RSMRL, and ASMRL are compared. Fig. 2(a) compares the position tracking curves of TSMRL, RSMRL, and ASMRL, demonstrating the superior tracking speed of the proposed ASMRL. Fig. 2(b) shows the phase trajectory of the system state from $s_0 \rightarrow s$. It can be seen that ASMRL has a faster convergence speed than TSMRL and RSMRL. Fig. 2(c) presents the control inputs for all three methods: TSMRL exhibits pronounced chattering; RSMRL demonstrates moderate oscillations; ASMRL achieves near-complete chattering suppression. Fig. 2(d) shows the system state convergence process of the three arrival laws, in which the system convergence accuracies of TSMRL and RSMRL are 0.0029 and 0.0014, respectively, and ASMRL is nearly zero. Collectively, ASMRL demonstrates marked improvements in convergence speed, steady-state error reduction, and chattering mitigation.

4. SPMSM SPEED CONTROL SYSTEM ASMC REALIZATION

4.1. Design of Speed Controller Based on the ASMRL

The design objective of a robust sliding mode velocity controller is to mitigate the impact of external load disturbances and internal parameter variations, where the entire system disturbance $d(t)$ is integrated into Eq. (2) as follows:

$$\dot{\omega}_{\mathrm{m}} = \frac{3}{2} P_n \psi_f i_q - \frac{B}{J}\omega_{\mathrm{m}} - \frac{1}{J} d(t) \quad (36)$$

For the design of the sliding mode controller, the motor-speed error and its derivative are formulated as follows:

$$\begin{cases} x_1 = \omega_{ref} - \omega_{\mathrm{m}} = e \\ x_2 = \dot{x}_1 = \dot{\omega}_{ref} - \dot{\omega}_{\mathrm{m}} = \dot{e} \end{cases} \quad (37)$$

where ω_{ref} is the speed reference value, and ω_m is the actual speed feedback value.

To mitigate system chattering and enhance dynamic response, this paper develops a non-singular fast terminal sliding mode surface (NFTSMS) from the TSMS, formulated as follows:

$$s = e + \beta_1 |e|^{\eta} \operatorname{sign}(e) + \beta_2 |\dot{e}|^{\gamma} \operatorname{sign}(\dot{e}) \quad (38)$$

where β_1 and β_2 are gain coefficients of the nonlinear terms; $\beta_1, \beta_2 > 0$, η, and γ are fractional power parameters with $0 < \eta < 1$ and $1 < \gamma < 2$; $\operatorname{sign}(\cdot)$ is a sign function to ensure the directionality of the slip mode surface.

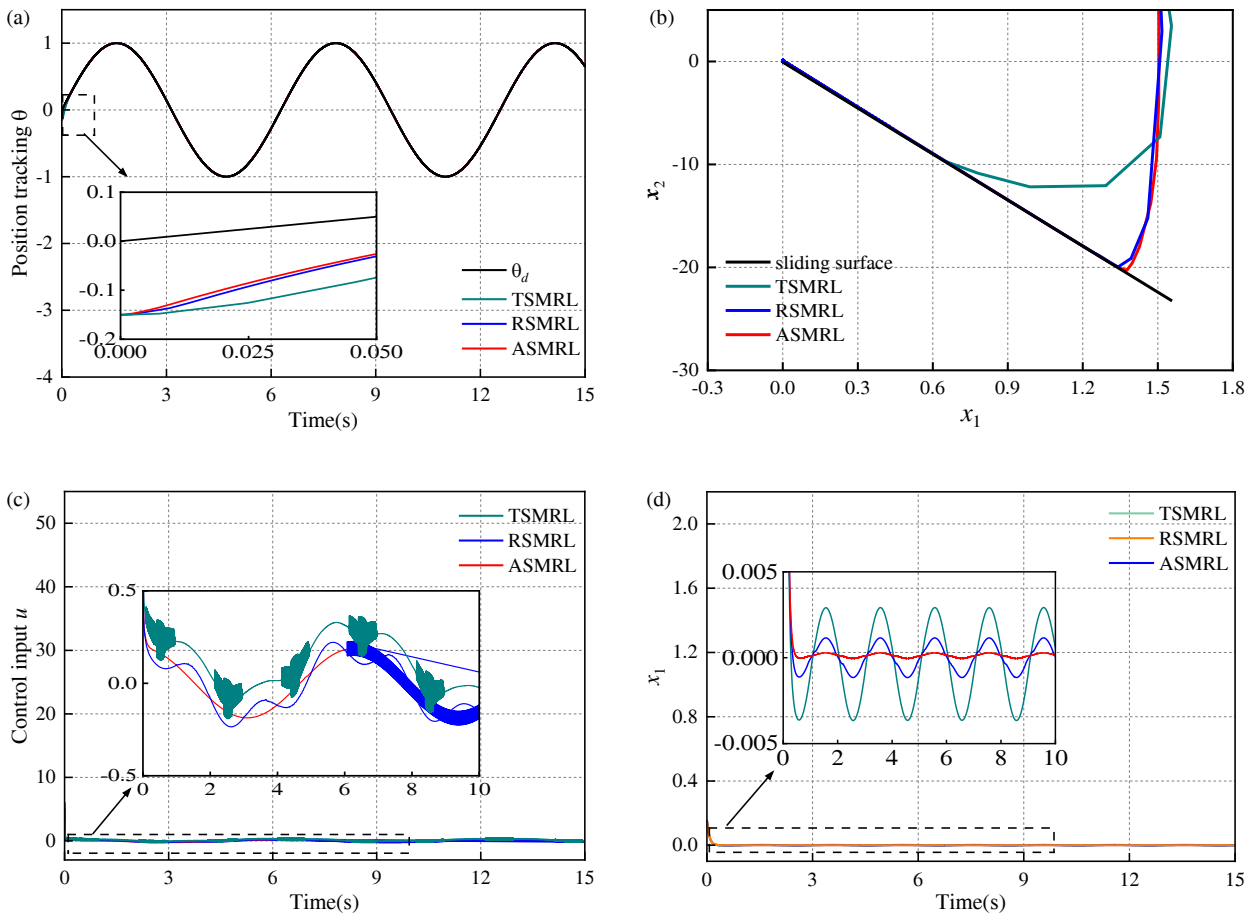

FIGURE 2. Performance comparison among TSMRL, RSMRL, and ASMRL. (a) Position tracking. (b) Phase trajectory. (c) Control input. (d) System state convergence process.

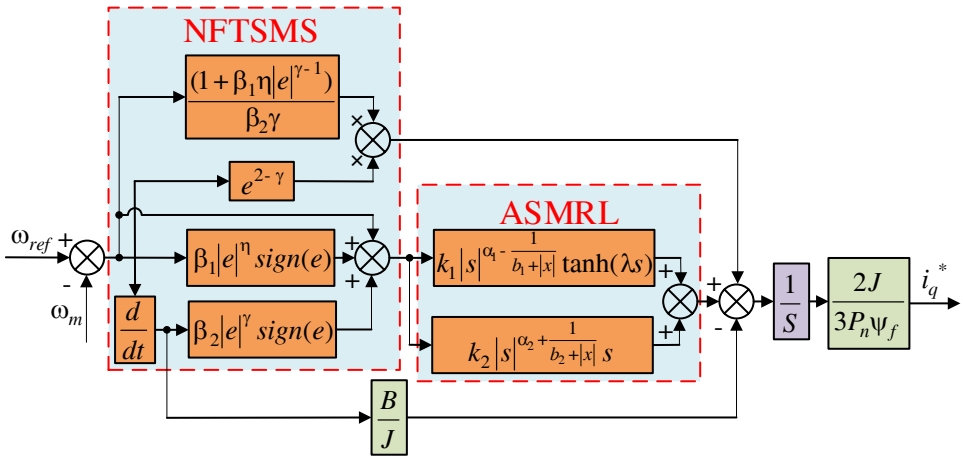

FIGURE 3. Structure block diagram of ASMC.

The derivative of the NFTSMS is:

$$\dot{s} = \dot{e} + \beta_1 \eta \left|e\right|^{\eta-1} \dot{e} + \beta_2 \gamma \left|\dot{e}\right|^{\gamma-1} \ddot{e} \tag{39}$$

Figure 3 illustrates the block diagram of the adaptive SMC (ASMC). To further attenuate sliding mode chattering, the ASMRL proposed in this study, integrated with Eqs. (36)–(39), yields the current reference value i_q^* as follows:

$$\begin{aligned} i_q^* = & \frac{2J}{3P_n\psi_f} \int_0^t \left[k_1 \left|s\right|^{\alpha_1 - \frac{1}{b_1+|x|}} \tanh\left(\lambda s\right) \right. \\ & + k_2 \left|s\right|^{\alpha_2 + \frac{1}{b_2+|x|}} s \\ & \left. + \frac{\left(1+\beta_1\eta\left|e\right|^{\eta-1}\right)}{\beta_2\gamma} \dot{e}^{2-\gamma} - \frac{B}{J}\dot{e} \right] dt \end{aligned} \tag{40}$$

4.2. Stability Proof of the ASMC

To verify that the ASMC, a speed control system is designed so that the speed error of the SPMSM converges to 0 in a finite time, and the stability of the system can be analyzed using the Lyapunov function. The Lyapunov function is defined as follows:

$$V = \frac{1}{2}s^2 \tag{41}$$

The derivation of Eq. (41) gives:

$$\begin{aligned}\dot{V} =& s\dot{s} = s(\dot{e} + \beta_1\eta\,|e|^{\eta-1}\,\dot{e} + \beta_2\gamma\,|\dot{e}|^{\gamma-1}\,\ddot{e})\\ =& s\Bigg[\dot{e} + \beta_1\eta\,|e|^{\eta-1}\,\dot{e} + \beta_2\gamma\,|\dot{e}|^{\gamma-1}\\ &\left(-\frac{(1+\beta_1\eta\,|e|^{\eta-1})}{\beta_2\gamma}\dot{e}^{2-\gamma}\right)\\ &-k_1\,|s|^{\alpha_1-\frac{1}{b_1+|x|}}\tanh(\lambda s) - k_2\,|s|^{\alpha_2+\frac{1}{b_2+|x|}}\,s\Bigg]\\ =&\beta_2\gamma\,|\dot{e}|^{\gamma-1}\,s(-k_1\,|s|^{\alpha_1-\frac{1}{b_1+|x|}}\tanh(\lambda s)\\ &-k_2\,|s|^{\alpha_2+\frac{1}{b_2+|x|}}\,s)\end{aligned} \tag{42}$$

Considering that $\beta_2\gamma\,|\dot{e}|^{\gamma-1} > 0$, k_1 and k_2 are all positive constants. It follows that:

$$\dot{V} \le 0 \tag{43}$$

This proves that the speed control system ASMC is stable.

5. REALIZATION OF SMC-GNFTSMO BASED SPEED CONTROL SYSTEM

5.1. Design of GNFTSMO

As demonstrated in Eq. (4), the entire system disturbance $d(t)$ is incorporated into the sliding-mode speed controller designed via the NFTSMS. Theorem 2 establishes that $d(t)$ adversely impacts the speed accuracy of the SPMSM control system. To enhance system robustness, this paper proposes a GNFTSMO to estimate perturbation magnitude in the SPMSM system, employing feedforward compensation for improved disturbance rejection.

The state-space equations are obtained using the mechanical angular speed ω_m and entire system disturbance $d(t)$ as variables:

$$\begin{bmatrix}\dot{\omega}_m\\ \dot{d}(t)\end{bmatrix} = \begin{bmatrix}-\frac{B}{J} & -\frac{1}{J}\\ 0 & 0\end{bmatrix}\begin{bmatrix}\omega_m\\ d(t)\end{bmatrix} + \begin{bmatrix}\frac{1}{J}\\ 0\end{bmatrix}T_e \tag{44}$$

ω_m and $d(t)$ were employed as observations to derive the following equation for the GNFTSMO:

$$\begin{bmatrix}\dot{\hat{\omega}}_m\\ \dot{\hat{d}}(t)\end{bmatrix} = \begin{bmatrix}-\frac{B}{J} & -\frac{1}{J}\\ 0 & 0\end{bmatrix}\begin{bmatrix}\hat{\omega}_m\\ \hat{d}(t)\end{bmatrix} + \begin{bmatrix}\frac{1}{J}\\ 0\end{bmatrix}T_e + \begin{bmatrix}1\\ g\end{bmatrix}h(e_\omega) \tag{45}$$

where g is the observer gain; $h(e_m)$ represents the sliding mode control law for the observer error; $\hat{\omega}_m$ and $\hat{d}(t)$ are the observations of ω_m and $d(t)$, respectively.

The speed observation error e_m and the total system disturbance observation error e_d are defined as:

$$\begin{cases}e_\omega = \omega_m - \hat{\omega}_m\\ e_d = d(t) - \hat{d}(t)\end{cases} \tag{46}$$

From Eq. (44) to Eq. (46), the error equation of the observer is obtained as:

$$\begin{bmatrix}\dot{e}_\omega\\ \dot{e}_d\end{bmatrix} = \begin{bmatrix}-\frac{B}{J} & -\frac{1}{J}\\ 0 & 0\end{bmatrix}\begin{bmatrix}e_\omega\\ e_d\end{bmatrix} - \begin{bmatrix}1\\ g\end{bmatrix}h(e_\omega) \tag{47}$$

For GNFTSMO, considering $-e_d/J$ as the disturbance term, Eq. (39) is chosen as the sliding mode surface, and the reaching law $\dot{s} = \tau\text{sign}(s)$ is selected, which combines Eq. (47) to derive the control law.

$$h(e_\omega) = \int_0^t\left[\frac{(1+\beta_1\eta\,|e_\omega|^{\eta-1})}{\beta_2\gamma}\dot{e}_\omega^{2-\gamma} - \frac{B}{J}\dot{e}_\omega + \tau\text{sign}(s)\right]dt \tag{48}$$

where τ denotes a positive constant, by adjusting the design parameters appropriately, and GNFTSMO can obtain satisfactory tracking effect. Fig. 4 is the structure diagram of GNFTSMO.

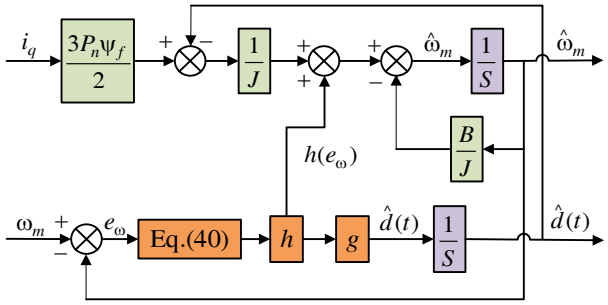

FIGURE 4. Structure block diagram of the GNFTSMO.

5.2. Stability Proof of the GNFTSMO

Proof of convergence of GNFTSMO, the Lyapunov stability condition, is $\dot{V} = s\dot{s} \le 0$, i.e., the system trajectory arrives at the sliding mode surface under the action of $h(e_m)$, and the observation error converges to zero, to satisfy the following equation:

$$\begin{cases}\dot{s} = s = 0\\ \dot{e}_\omega = e_\omega = 0\end{cases} \tag{49}$$

From Eq. (47), it follows that:

$$\dot{e}_d = \frac{g}{J}e_d \tag{50}$$

Solving the differential equation for Eq. (51) gives:

$$e_d = c_d e^{\frac{g}{J}t} \tag{51}$$

where c_d is a constant. For the system perturbation error e_d to converge, the gain $g < 0$ must be satisfied.

The Lyapunov function is derived as:

$$\begin{aligned}\dot{V} &= s\dot{s} = s\left(\dot{e}_\omega + \beta_1\eta\left|e_\omega\right|^{\eta-1}\dot{e}_\omega + \beta_2\gamma\left|\dot{e}_\omega\right|^{\gamma-1}\ddot{e}_\omega\right) \\ &= s\left(-\tau\text{sign}(s)\right) \\ &= -\tau\left|s\right| \le 0\end{aligned} \tag{52}$$

With the above designed GNFTSMO, the entire system disturbance $d(t)$ of the system can be estimated, and Eq. (4) can be rewritten as:

$$\begin{aligned}i_q^* = &\frac{2J}{3P_n\psi_f}\int_0^t\left[k_1\left|s\right|^{\alpha_1-\frac{1}{b_1+|x|}}\tanh\left(\lambda s\right)\right. \\ &+ k_2\left|s\right|^{\alpha_2+\frac{1}{b_2+|x|}}s \\ &\left.+\frac{\left(1+\beta_1\eta\left|e\right|^{\eta-1}\right)}{\beta_2\gamma}\dot{e}^{2-\gamma} - \frac{B}{J}\dot{e}\right]dt + \hat{d}\left(t\right)\end{aligned} \tag{53}$$

The control structure of the SPMSM speed regulation system based on the proposed ASMC-GNFTSMO method is shown in Fig. 5.

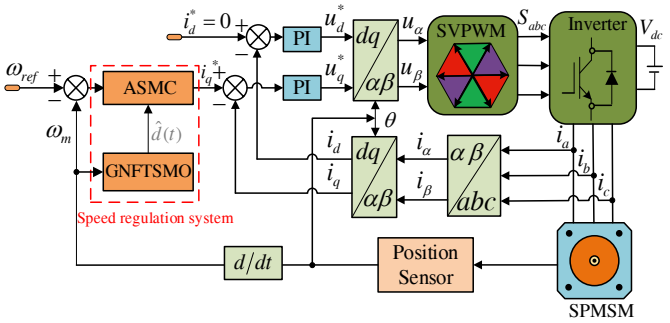

FIGURE 5. Structure diagram of SPMSM speed control system.

6. SIMULATION AND EXPERIMENT RESULTS

6.1. Simulation Verification

Prior to the comparison, the TSMRL-based control was designated TSMC and the RSMRL-based control designated RSMC. In order to verify the effectiveness and correctness of the proposed method, a simulation model was built based on the MATLAB/Simulink platform. A comparison of the control strategies with those of TSMC, RSMC, ASMC, and ASMC based on GNFTSMO is then made. The vector control mode with $i_d = 0$ is adopted; the simulation step size is 1e-5s; and the space vector pulse width modulation switching frequency is 10 kHz. The SPMSM parameters utilized in the simulation are enumerated in Table 1, while the control parameters of all the control strategies are shown in Table 2.

The observed plot of load disturbance for the GNFTSMO is presented in Fig. 6. It can be noted that the response curve of GNFTSMO effectively suppresses pulsations following the load disturbance, resulting in a smooth output. The locally

TABLE 1. Main parameters of the simulation.

Symbol	Parameters	Value
U_{dc}	DC voltage	311 V
ψ_f	Flux linkage	0.175 Wb
R_S	Stator resistance	2.875 Ω
J	Rotational inertia	0.003 kg · m^2
B	Damping coefficient	0.008 N · m · s
L_S	dq-axis inductance	8.5 mH
P_n	Number of pole pairs	4

TABLE 2. Parameters of the control system.

Control strategy	Parameter value
TSMC	$k_1 = 2200, k_2 = 5000, \beta_1 = 4,$ $\beta_2 = 0.0009, \eta = 0.4, \gamma = 1.5,$
RSMC	$k_1 = 2200, k_2 = 5000, \alpha = 100, \beta = 150,$ $a = 0.7, b = 0.001, \lambda = 1, \beta_1 = 4,$ $\beta_2 = 0.0009, \eta = 0.4, \gamma = 1.5,$
ASMC	$k_1 = 2200, k_2 = 5000, \alpha_1 = 0.3, \alpha_2 = 0.6,$ $a_1 = 1, b_1 = 2, \lambda = 1, \beta_1 = 4, \beta_2 = 0.0009,$ $\eta = 0.4, \gamma = 1.5,$
ASMC-GFNTSMO	$k_1 = 2200, k_2 = 5000, \alpha_1 = 0.3, \alpha_2 = 0.6,$ $a_1 = 1, b_1 = 2, \lambda = 1, \beta_1 = 4, \beta_2 = 0.0009,$ $\eta = 0.4, \gamma = 1.5, g = -1, \tau = 0.56$

zoomed-in plot reveals that the response time of GNFTSMO is 0.0042 seconds, indicating its excellent tracking performance.

Figure 7 depicts the no-load starting speed response of the system under a 01000 rpm ramp reference. The results demonstrate that TSMC exhibits the longest settling time and highest overshoot, followed by RSMC. In contrast, ASMC and ASMC-GNFTSMO achieve near-zero overshoot, with ASMC-GNFTSMO achieving the fastest response time. These results confirm that the proposed ASMC-GNFTSMO methodology effectively suppresses overshoot and delivers superior dynamic performance.

To validate the anti-disturbance implementation of the proposed strategy, the load was abruptly increased to 8 N · m when the system was operated for 0.2 s and the load was abruptly decreased to 0 N · m at 0.4 s. As demonstrated in Fig. 8 and further supported by Table 3, the ASMC-GNFTSMO control exhibited the fastest speed and torque response, along with the most effective anti-disturbance performance. As demonstrated in Fig. 8(a), the TSMC exhibited the most significant overshoot of 53.2 rpm and the longest adjustment time during load changes; the RSMC demonstrated an overshoot of 24.8 rpm; the ASMC exhibited a maximum overshoot of 18.3 rpm and rapidly returned to the nominal speed with optimal anti-disturbance. In contrast, the speed drop of ASMC-GNFTSMO with disturbance compensation is less than that of ASMC without disturbance compensation, and the recovery time of ASMC-GNFTSMO is the shortest at 35 ms (Overshoot 1 is the no-load start-up overshoot; Overshoot 2 is the add-load overshoot; Overshoot 3 is the un-load overshoot; Adjustment time 1 is the

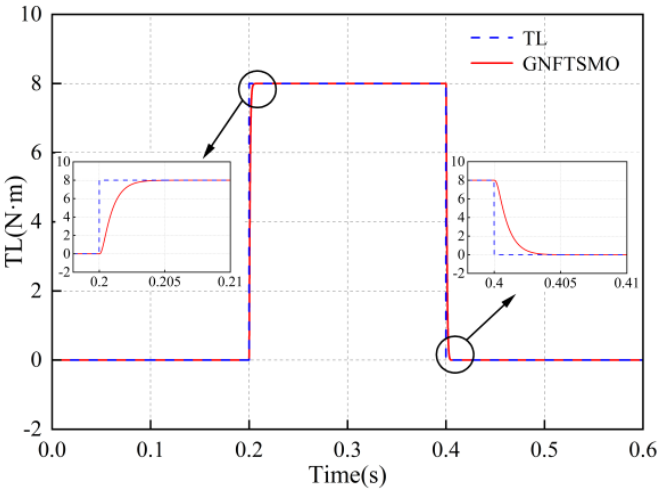

FIGURE 6. Load disturbance observation.

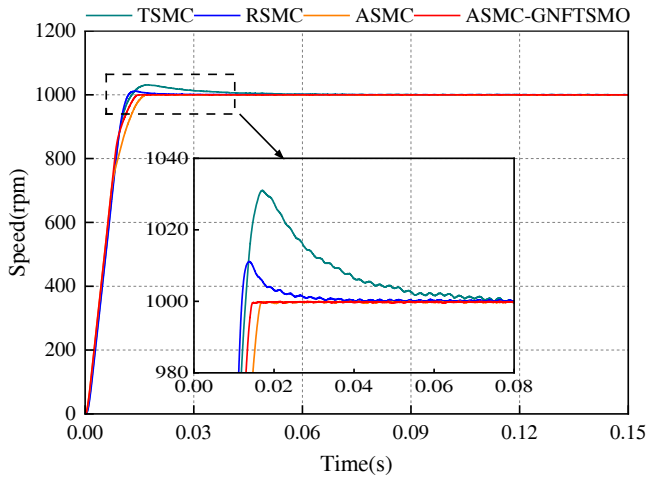

FIGURE 7. No-load start-up speed responses.

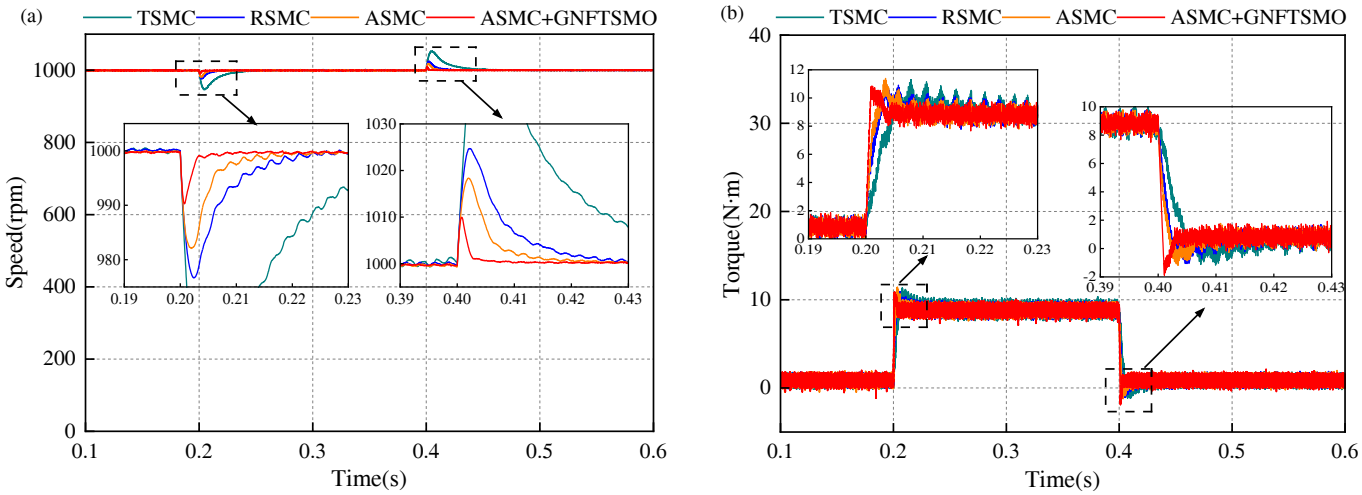

FIGURE 8. Speed and torque responses under abrupt load change. (a) Speed responses. (b) Torque responses.

TABLE 3. SPMSM system performance under simulation.

Performance Indicators	TSMC	RSMC	ASMC	ASMC-GNFTSMO
Speed error	0.8 rpm	0.4 rpm	0.2 rpm	0.18 rpm
Overshoot 1	31 rpm	11.3 rpm	0 rpm	0 rpm
Overshoot 2	52.5 rpm	23.2 rpm	17.8 rpm	9.4 rpm
Overshoot 3	53.2 rpm	24.8 rpm	18.3 rpm	9.8 rpm
Adjustment time 1	78 ms	42 ms	16.7 ms	14.8 ms
Adjustment time 2	55 ms	23.5 ms	14 ms	3.5 ms
Adjustment time 3	58 ms	26 ms	17 ms	4 ms

no-load start-up adjustment time; Adjustment time 2 is the add-load adjustment time; Adjustment time 3 is the un-load adjustment time.)

To verify the robustness of the proposed control method, the reference rotational speed was varied between 800 and 1200 rpm, as illustrated in Fig. 9. This figure indicates that methods TSMC and RSMC exhibit significant overshoot relative to method ASMC, whereas method ASMC demonstrates notably slower response speed than method ASMC-GNFTSMO. These comparative results confirm the superior robustness of the proposed controller during variable-speed operation.

The conclusion drawn from this analysis is that the proposed control strategy demonstrates both dynamic and anti-interference performances.

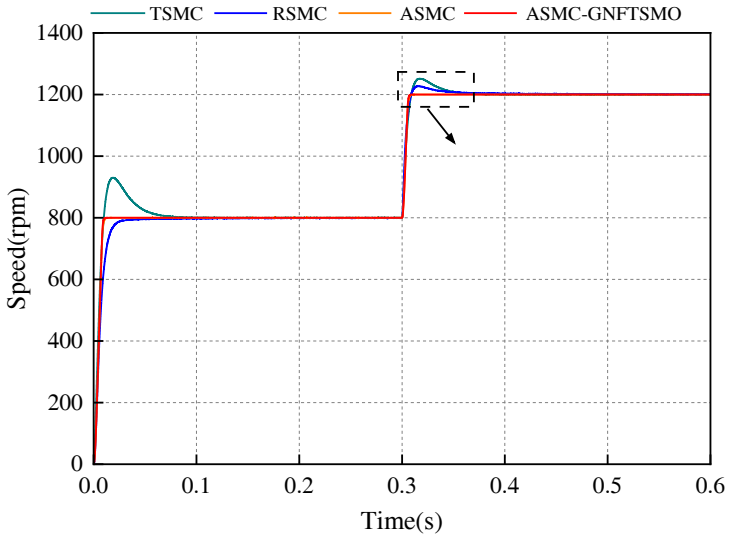

FIGURE 9. Simulation curves during speed variation.

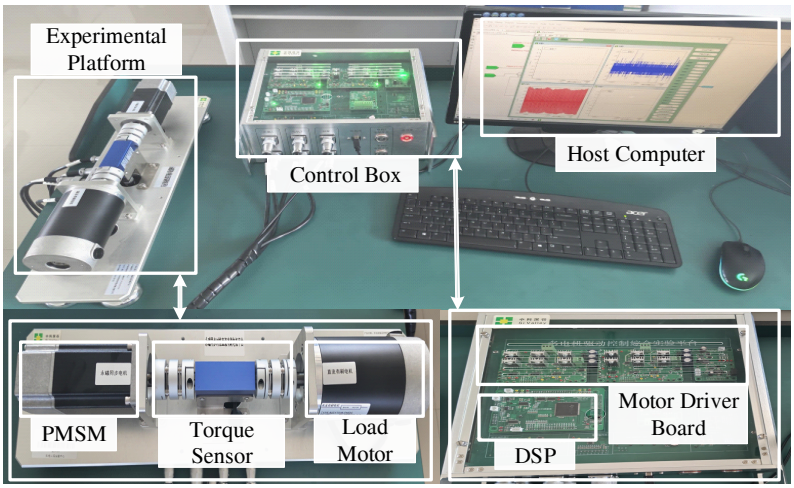

FIGURE 10. Experimental platform.

6.2. Experiment Verification

This section validates the feasibility and effectiveness of the proposed ASMC-GNFTSMO method on a 0.4 kW SPMSM experimental platform (Fig. 10), with detailed analysis of experimental outcomes across diverse operating conditions. The experimental setup comprises a direct-drive SPMSM coupled with a load motor, a dedicated motor control module, and a torque sensor. The control algorithms were executed on a DSP TMS320F28335, supported by a PC, DC power supply, Analog to Digital Converter (ADC), current sensors, a drive power supply, and signal conditioning and adapter boards. The inverter has an operating frequency of 10 kHz, a rated torque of 1.27 N · m, a rated voltage of 48 V, and a rated current of 12.5 A. A 2500-wire incremental rotary encoder is mounted on the end of the motor shaft to measure the digital position to obtain the SPMSM speed.

Figure 11 shows the experimental waveforms of speed, torque, and A-phase current for the four control methods during no-load starting. From Fig. 11(a) to Fig. 11(d), as evident in Fig. 11(a) to Fig. 11(d), the overshoots of TSMC and RSMC are 50 rpm and 18 rpm, respectively. In contrast, ASMC and ASMC-GNFTSMO demonstrate a negligible overshoot. The response times of TSMC, RSMC, ASMC, and ASMC-GNFTSMO are 0.556 s, 0.512 s, 0.495 s, and 0.454 s, respectively. Meanwhile, ASMC-GNFTSMO has a significant effect in suppressing torque pulsation.

Figure 12 gives the histograms of the experimental performance comparison of the motor startup, and the speed overshoot and response time are selected as the comparison terms. As shown in Fig. 12, TSMC overshoot is observed to be greater than that of RSMC, while ASMC and ASMC-GNFTSMO exhibit negligible overshoot. The response time from slow to fast is TSMC, RSMC, ASMC, ASMC-GNFTSMO. This finding indicates that the proposed control method is capable of enhancing the system's responsiveness and effectively mitigating speed and torque pulsations.

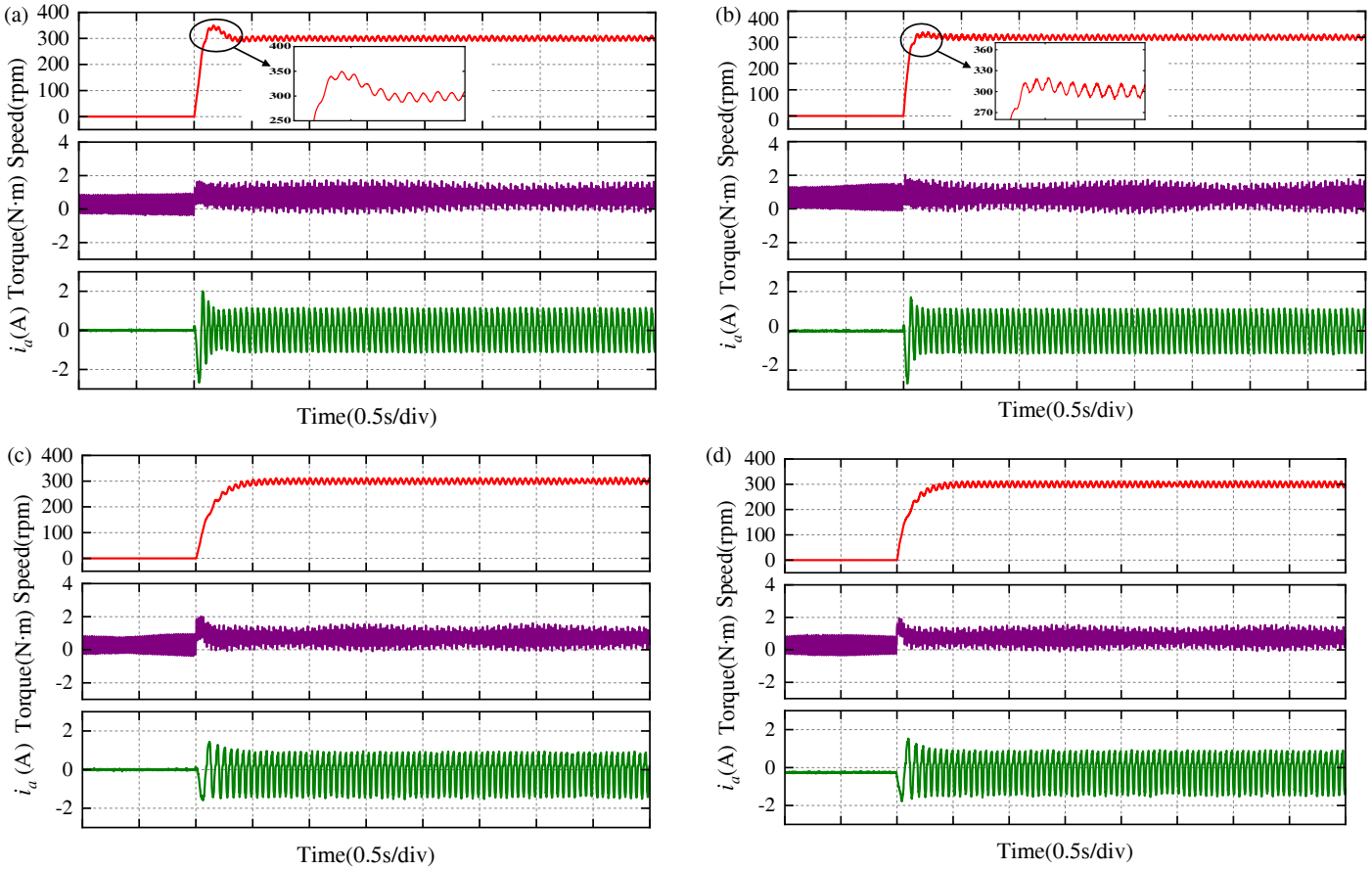

FIGURE 11. Comparison of speed, torque, and A-phase current of SPMSM under no-load condition. (a) TSMC. (b) RSMC. (c) ASMC. (d) ASMC-GNFTSMO.

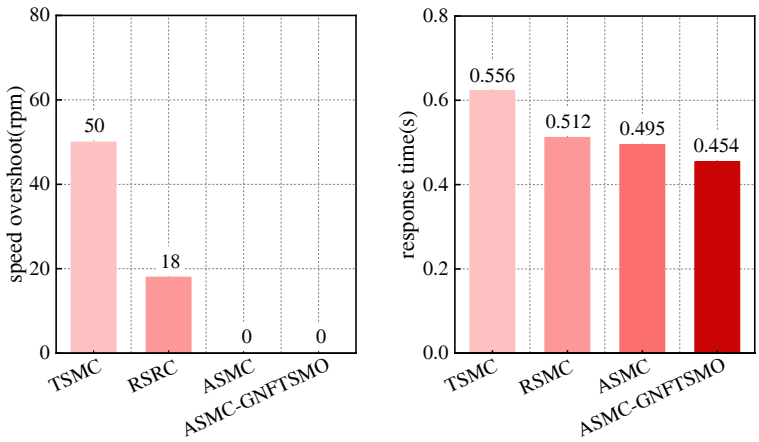

FIGURE 12. Performance comparison of four control methods under startup.

Figure 13 shows the experimental waveforms of speed, torque, and A-phase current during loading and unloading with different control methods. From Fig. 13 and Table 4, it can be seen that the proposed ASMC method can suppress the load disturbances well; the speed drop during loading is 29.09% and 35.56% of TSMC and RSMC, respectively; the speed rise during load shedding is 27.52% and 34.09% of TSMC and RSMC, respectively. In addition, the torque pulsation and speed fluctuation of ASMC during loading are also smaller than those of TSMC and RSMC. The ASMC-GNFTSMO method further improves the above indexes, which verifies that the control method proposed in this paper has better disturbance suppression capability. (Overshoot 1 is the add-load overshoot; Overshoot 2 is the un-load overshoot; Adjustment time 1 is the add-load adjustment time; Adjustment time 2 is the un-load adjustment time.)

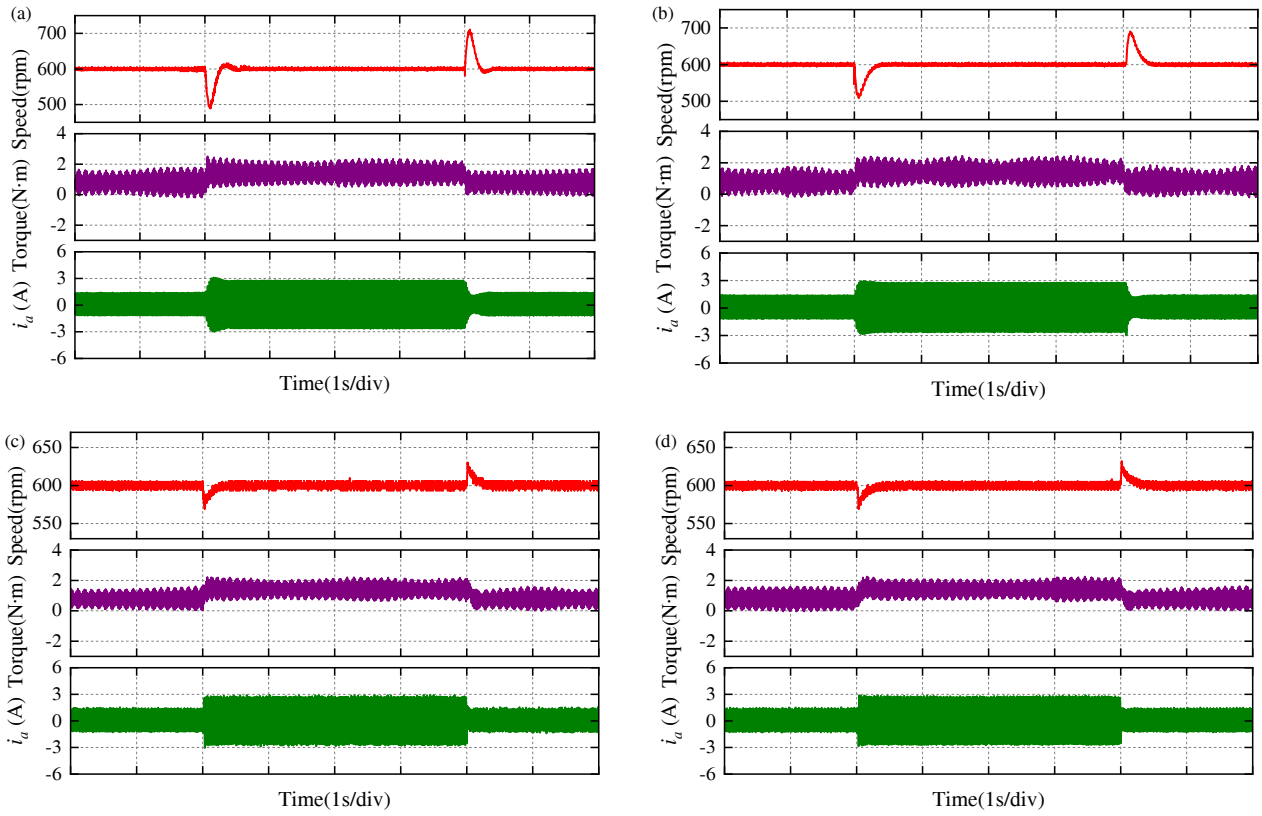

FIGURE 13. Comparison of speed, torque, and A-phase current under sudden loading and unloading conditions. (a) TSMC. (b) RSMC. (c) ASMC. (d) ASMC-GNFTSMO.

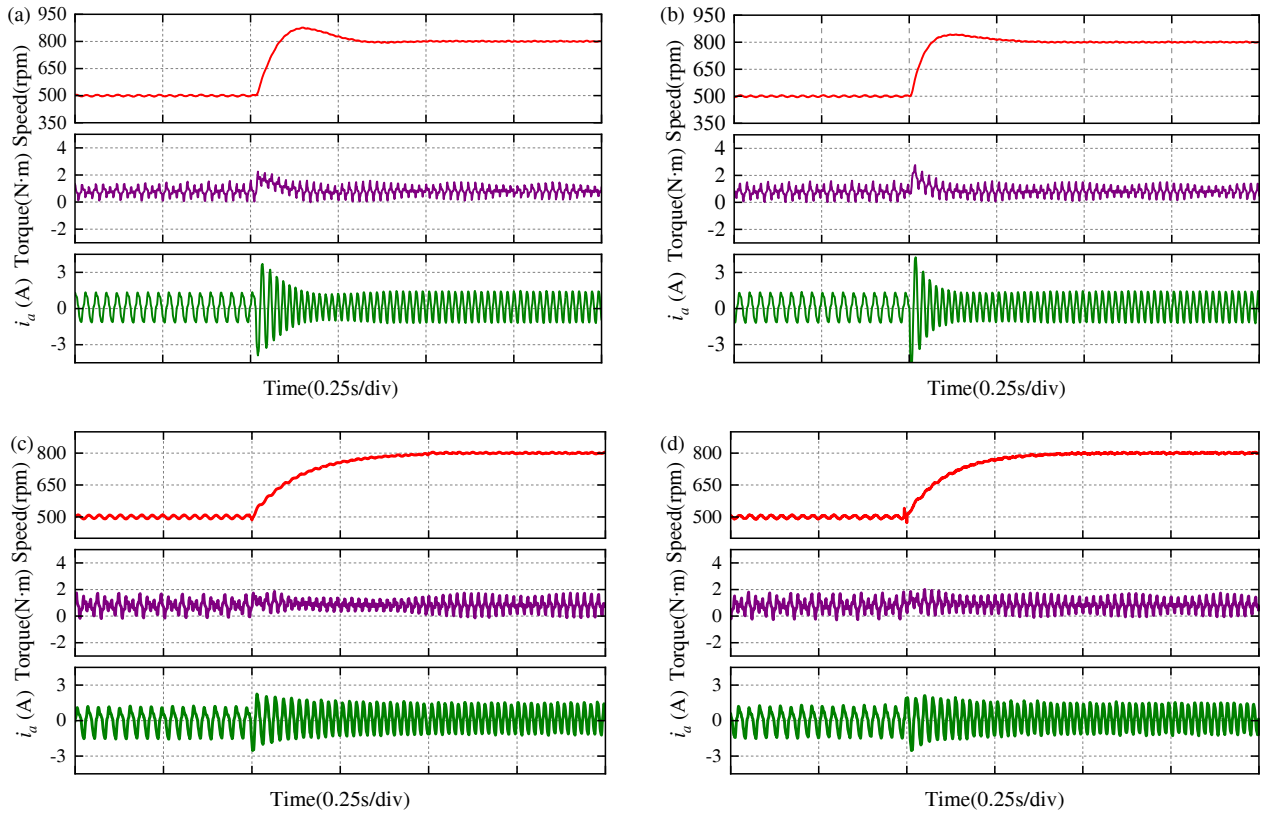

FIGURE 14. The speed, torque, and A-phase current response of different methods. (a) TSMC. (b) RSMC. (c) ASMC. (d) ASMC-GNFTSMO.

TABLE 4. Performance comparison of four control methods sunder step load condition.

Performance Indicators	TSMC	RSMC	ASMC	ASMC- GNFTSMO
Overshoot 1	110 rpm	90 rpm	32 rpm	30 rpm
Overshoot 2	109 rpm	88 rpm	30 rpm	29 rpm
Adjustment time 1	0.631 s	0.549 s	0.366 s	0.343 s
Adjustment time 2	0.611 s	0.573 s	0.382 s	0.362 s

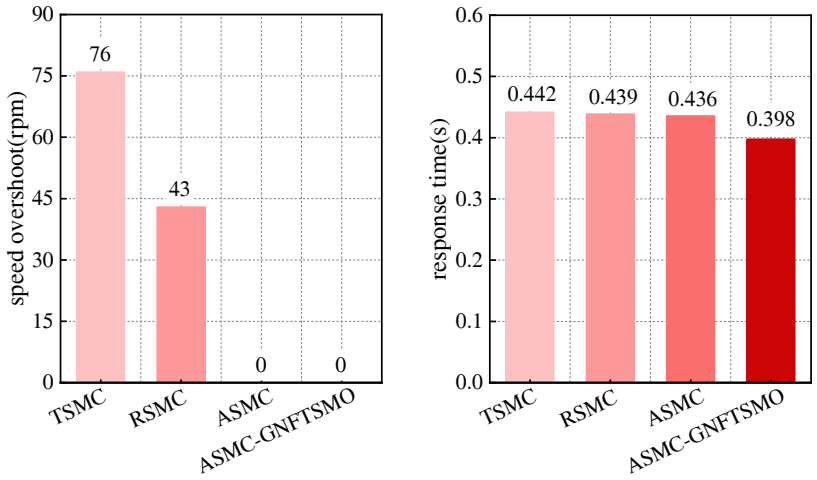

FIGURE 15. Performance comparison of four control methods under variable speed.

Figure 14 shows the experimental comparison of the four control methods for increasing the speed from 500 rpm to 800 rpm. From Fig. 14 and Fig. 15, it can be seen that the response times of the proposed ASMC-GNFTSMO and ASMC methods are slightly smaller than that of the RSMC method and much smaller than that of the TSMC method during the speed change, which confirms the rapidity of the proposed methods. Compared with TSMC and RSMC methods, the speed and torque pulsations of the ASMC-GNFTSMO and ASMC methods are greatly reduced, which verifies that the proposed methods are able to greatly reduce the steady-state jitter.

7. CONCLUSION

To improve the dynamics of the SPMSM speed governing system, this paper proposes an adaptive state-variable-based reaching law, which has the advantages of reducing the steady-state error and weakening the jitter while arriving at the sliding-mode surface quickly compared with the existing sliding-mode reaching law. In order to further reduce the steady-state error of the SPMSM speed control system, this paper designs a global non-singular fast terminal sliding-mode observer on the basis of the speed controller designed with the proposed reaching law, which is able to feedforward compensate the disturbance of the speed controller, and improves the rapidity and anti-interference of the speed control system. Simulated and experimental results show that the proposed method can effectively improve the response speed of the system, suppress the torque-speed pulsation, and improve the anti-interference performance to external loads.

ACKNOWLEDGEMENT

This work was supported in part by the Natural Science Research Project of Anhui Educational Committee under No. 2022AH051583.

REFERENCES

[1] Wang, H., L. Shi, Z. Man, J. Zheng, S. Li, M. Yu, C. Jiang, H. Kong, and Z. Cao, "Continuous fast nonsingular terminal sliding mode control of automotive electronic throttle systems using finite-time exact observer," *IEEE Transactions on Industrial Electronics*, Vol. 65, No. 9, 7160–7172, 2018.

[2] Alonso, D. F., Y. Kang, D. F. Laborda, M. M. Gómez, D. D. Reigosa, and F. Briz, "Permanent magnet synchronous machine torque estimation using low cost hall-effect sensors," *IEEE Transactions on Industry Applications*, Vol. 57, No. 4, 3735–3743, 2021.

[3] Chen, S., W. Ding, X. Wu, R. Hu, and S. Shi, "Novel random high-frequency square-wave and pulse voltage injection scheme-based sensorless control of IPMSM drives," *IEEE Journal of Emerging and Selected Topics in Power Electronics*, Vol. 11, No. 2, 1705–1721, 2023.

[4] Wang, C. and Z. Q. Zhu, "Fuzzy logic speed control of permanent magnet synchronous machine and feedback voltage ripple reduction in flux-weakening operation region," *IEEE Transactions on Industry Applications*, Vol. 56, No. 2, 1505–1517, 2020.

[5] Yuan, L., M.-l. Chen, J.-q. Shen, and F. Xiao, "Current harmonics elimination control method for six-phase PM synchronous motor drives," *ISA Transactions*, Vol. 59, 443–449, 2015.

[6] Guo, X., S. Huang, Y. Peng, K. Lu, S. Huang, D. Luo, and X. Wu, "An improved integral sliding mode control for PMSM drives

based on new variable rate reaching law with adaptive reduced-order PI observer," *IEEE Transactions on Transportation Electrification*, Vol. 9, No. 3, 4503–4516, 2023.

[7] Li, T., X. Chen, J. Liu, and J. Yu, "Fixed-time adaptive fuzzy control via filter and observer for uncertain nonlinear systems with disturbances and its application in PMSMs," *IEEE Transactions on Industrial Electronics*, Vol. 71, No. 11, 14 712–14 721, 2024.

[8] Lu, X., F. Wang, Z. Liu, R. Zhu, and C. L. P. Chen, "Adaptive fuzzy fixed-time control for nonlinear systems with input and output quantization," *IEEE Transactions on Automation Science and Engineering*, Vol. 22, 5158–5169, 2025.

[9] Xia, J. and H. Ouyang, "Chattering free sliding-mode controller design for underactuated tower cranes with uncertain disturbance," *IEEE Transactions on Industrial Electronics*, Vol. 71, No. 5, 4963–4975, 2024.

[10] Steinberger, M., M. Horn, and A. Ferrara, "Adaptive control of multivariable networked systems with uncertain time delays," *IEEE Transactions on Automatic Control*, Vol. 67, No. 1, 489–496, 2022.

[11] Masoudi, H., A. Kiyoumarsi, S. M. Madani, and M. Ataei, "Torque ripple reduction of nonsinusoidal brushless dc motor based on super-twisting sliding mode direct power control," *IEEE Transactions on Transportation Electrification*, Vol. 9, No. 3, 3769–3779, 2023.

[12] Zhang, Z., X. Yang, W. Wang, K. Chen, N. C. Cheung, and J. Pan, "Enhanced sliding mode control for PMSM speed drive systems using a novel adaptive sliding mode reaching law based on exponential function," *IEEE Transactions on Industrial Electronics*, Vol. 71, No. 10, 11 978–11 988, 2024.

[13] Feng, Y., J. Zheng, X. Yu, and N. V. Truong, "Hybrid terminal sliding-mode observer design method for a permanent-magnet synchronous motor control system," *IEEE Transactions on Industrial Electronics*, Vol. 56, No. 9, 3424–3431, 2009.

[14] Zhu, Z., Y. Lin, and Y. Zhang, "Adaptive quasi-fixed-time integral terminal sliding mode control for nonlinear systems," *IEEE Transactions on Circuits and Systems II: Express Briefs*, Vol. 71, No. 3, 1366–1370, 2024.

[15] Xu, W., A. K. Junejo, Y. Liu, and M. R. Islam, "Improved continuous fast terminal sliding mode control with extended state observer for speed regulation of PMSM drive system," *IEEE Transactions on Vehicular Technology*, Vol. 68, No. 11, 10 465–10 476, 2019.

[16] Zhang, L., R. Tao, Z.-X. Zhang, Y.-R. Chien, and J. Bai, "PMSM non-singular fast terminal sliding mode control with disturbance compensation," *Information Sciences*, Vol. 642, 119040, 2023.

[17] Wang, Y., Y. Feng, X. Zhang, and J. Liang, "A new reaching law for antidisturbance sliding-mode control of PMSM speed regulation system," *IEEE Transactions on Power Electronics*, Vol. 35, No. 4, 4117–4126, 2020.

[18] Zhu, J., X. Cao, Q. Ge, and D. Zeng, "Adaptive-SMO-based traction force fluctuation suppression strategy considering suspension system for high-speed maglev train," *IEEE Transactions on Industrial Electronics*, Vol. 71, No. 3, 2289–2299, 2024.

[19] Gao, X., Z. Ren, L. Zhai, Q. Jia, and H. Liu, "Two-stage switching hybrid control method based on improved PSO for planar three-link under-actuated manipulator," *IEEE Access*, Vol. 7, 76 263–76 273, 2019.

[20] Wang, C., F. Liu, J. Xu, and J. Pan, "An SMC-based accurate and robust load speed control method for elastic servo system," *IEEE Transactions on Industrial Electronics*, Vol. 71, No. 3, 2300–2308, 2024.

[21] Huang, J., S. Ri, T. Fukuda, and Y. Wang, "Notice of removal: A disturbance observer based sliding mode control for a class of underactuated robotic system with mismatched uncertainties," *IEEE Transactions on Automatic Control*, Vol. 64, No. 6, 2480–2487, 2019.

[22] Dai, B. and Z. Wang, "Disturbance observer-based sliding mode control using barrier function for output speed fluctuation constraints of PMSM," *IEEE Transactions on Energy Conversion*, Vol. 39, No. 2, 1192–1201, 2024.

[23] Lian, C., F. Xiao, S. Gao, and J. Liu, "Load torque and moment of inertia identification for permanent magnet synchronous motor drives based on sliding mode observer," *IEEE Transactions on Power Electronics*, Vol. 34, No. 6, 5675–5683, 2019.

[24] Gao, W. and J. C. Hung, "Variable structure control of nonlinear systems: A new approach," *IEEE Transactions on Industrial Electronics*, Vol. 40, No. 1, 45–55, 1993.

[25] Qu, Y., B. Zhang, H. Chu, H. Shen, J. Zhang, and X. Yang, "Sliding-mode anti-disturbance speed control of permanent magnet synchronous motor based on an advanced reaching law," *ISA Transactions*, Vol. 139, 436–447, 2023.

[26] Yu, J., P. Shi, C. Lin, and H. Yu, "Adaptive neural command filtering control for nonlinear MIMO systems with saturation input and unknown control direction," *IEEE Transactions on Cybernetics*, Vol. 50, No. 6, 2536–2545, 2020.

[27] Qu, S., W. Xu, J. Zhao, and H. Zhang, "Design and implementation of a fast sliding-mode speed controller with disturbance compensation for SPMSM system," *IEEE Transactions on Transportation Electrification*, Vol. 7, No. 4, 2611–2622, 2021.